

Transition magnon modes in thin ferromagnetic nanogratings

S. M. Kukhtaruk,^{1,2,*} A. W. Rushforth,³ F. Godejohann,¹ A. V. Scherbakov,¹ and M. Bayer¹

¹*Experimentelle Physik 2, Technische Universität Dortmund,
Otto-Hahn-Str. 4a, 44227 Dortmund, Germany.*

²*Department of Theoretical Physics, V.E. Lashkaryov Institute of Semiconductor Physics, 03028 Kyiv, Ukraine.*

³*School of Physics and Astronomy, University of Nottingham, Nottingham NG7 2RD, United Kingdom.*

This work presents micromagnetic simulations in ferromagnetic nanogratings for the full range of directions of an applied in-plane external magnetic field. We focus on the modification of the magnon mode characteristics when the magnetic field orientation is gradually changed between the classical Damon-Eshbach (DE) and backward-volume (BV) geometries. We found that in a specific range of field directions, the magnon mode parameters differ significantly from the parameters in the classical cases, namely, the modes are characterized by complex spatial distributions and have low group velocities. The center of this range corresponds to the direction of the external magnetic field, which gives the maximal nonuniform distribution of the static magnetization in the nanogratings.

I. INTRODUCTION

Magnonics is a rapidly developing direction of modern magnetism that uses spin waves (or magnons) for data transfer and processing [1–3]. Structures with spatially periodic magnetic properties, referred to as magnonic crystals [4–14], and periodically patterned ferromagnetic films, referred to as surface modulated magnonic crystals [15–26], take a central role in this field. The simplest pattern is a periodic set of grooves and wires that form a (nano-) grating (NG) structure which, despite its simple design, already shows prospective potential for multiple applications, e.g. magnonic transistors [27], switches [28–30], filters [15, 31], grating couplers [32], magnetic field generators [33] and detectors [34].

An essential feature of NG structures is the rich spectrum of magnon eigenmodes, which can be tuned by an external magnetic field, \mathbf{H}_{ext} . It consists of the modes with wave vector along the reciprocal wave vector of the NG (perpendicular to the grooves) with energy dispersions and spatial distributions significantly different from the case of a plain film (see e.g. [13, 25]). The dispersions determine the magnon modes' group velocities as well as the magnon band gaps' spectral positions and widths. The spatial profiles of the magnon modes define their excitation selectivity and the interaction with other periodic excitations, such as electromagnetic [5, 7–9, 20, 21, 24, 25] or elastic [35–37] waves. The excitation and interaction efficiencies depend on the spatial matching of the magnon modes and other wave excitations, and can be entirely suppressed in case of poor matching.

An essential fundamental phenomenon in magnonics is *nonreciprocity*, i.e. the difference in localization [38] and/or amplitude [39, 40] and/or frequency [13, 14, 22, 26, 41] of the spin waves with opposite directions of their wave vectors. In NG structures, magnons can possess asymmetric dispersions with indirect band gaps in the Brillouin zone [13, 22]. In this case, spin waves with

Bloch wavevectors at the center of the Brillouin zone are propagating waves. Thus, nonreciprocity provides the ability to excite propagating spin waves employing spatially homogeneous excitations.

The main experimental tools for studying magnons in NG structures are Brillouin light scattering [2, 5, 7–9, 42] and ferromagnetic resonance (FMR) [19–21, 24, 25, 43] spectroscopy. Traditionally, only two directions of \mathbf{H}_{ext} are studied: either perpendicular (the Damon-Eshbach (DE) geometry) or parallel (the backward-volume (BV) geometry) to the magnon wavevector. However, to the best of our knowledge, so far there is no information available about the main magnon characteristics in NG structures for intermediate directions of \mathbf{H}_{ext} .

While magnons in plain ferromagnetic films are well studied for any magnetic field direction [38, 44], the introduction of grooves not only fixes the magnon wave vector direction, but also leads to the generation of both static and dynamic demagnetizing fields, which strongly influence the magnon characteristics. For instance, the magnon spatial profiles and dispersions at 45° , i.e. in between the DE and BV geometries, are a priori not known, i.e., the question is whether this case is DE-like or BV-like? In addition, it is unclear how the transition between the DE and BV geometries is arranged, i.e., is the change of the mode characteristics smooth across the wide range or does it occur sharply for a specific magnetic field direction? Moreover, time-resolved experiments on excitation of a metallic ferromagnet by femtosecond laser pulses and detection of the coherent magnon response using the transient magneto-optical Kerr effect (MOKE) [33, 45–49] are typically performed at intermediate directions of \mathbf{H}_{ext} , where the excitation efficiency is maximal [48, 49]. Thus, an analysis of the magnons at intermediate directions of \mathbf{H}_{ext} providing answers to the above questions are required.

This paper presents a detailed theoretical analysis of magnons in a ferromagnetic NG for arbitrary directions of \mathbf{H}_{ext} . We focus on the main magnon characteristics including the spatial profiles, dispersions, and dependencies of the magnon frequencies on the direction and strength of \mathbf{H}_{ext} . We find that by changing the direction of the

* serhii.kukhtaruk@tu-dortmund.de

magnetic field continuously from DE geometry to BV geometry, the main magnon characteristics remain DE-like until the field direction enters a *transition range*, where the magnon characteristics are neither DE-like nor BV-like. When exiting this transition range, the magnon characteristics can be considered to be BV-like. We show that both the static magnetization and the demagnetizing field are critically important for the transition. The position of the transition range is defined by the particular direction of the external magnetic field, which corresponds to the maximal nonuniform distribution of the static magnetization in the NG. The width of the transition range is $\sim 25^\circ$. Therefore, by changing the magnetic field direction around the transition range one can switch between three different types of magnon modes and choose the magnon modes with the desired characteristics.

For the calculations, we use the COMSOL Multiphysics[®] software [50]. Our choice is based on the ability to solve and visualize the problem in both time and frequency domains with integration of a specific external impact, such as femtosecond laser excitation, monochromatic elastic waves, or picosecond strain pulses, which are widely used in time-resolved magnonic experiments (see e.g. [33, 45–49]).

The paper is organized as follows: The basic equations and used parameters are given in Sec. II. The steady-state situation is considered in Sec. III. The magnon characteristics are discussed in Secs. IV and V. The validity and applications are discussed in Sec. VI. The conclusions are summarized in Sec. VII.

II. BASIC EQUATIONS

The system under study is a NG structure that consists of infinitely long parallel grooves of depth h , separated by wires of width w . The NG is produced in a ferromagnetic film of thickness l , (see Fig. 1), located on a nonmagnetic substrate, which is not shown for simplicity. The NG period is d , and the width of the grooves is $d - w$. The external magnetic field, \mathbf{H}_{ext} , is applied in the structural plane of the ferromagnet at an angle φ_H between the grooves and \mathbf{H}_{ext} .

The magnetization \mathbf{M} in the ferromagnetic NG structure is described by the Landau-Lifshitz-Gilbert equation (see, e.g., [51–53]). It is convenient to introduce a normalized magnetization $\mathbf{m} = \mathbf{M}/M_s$, where M_s is the saturation magnetization and $|\mathbf{m}| = 1$. Moreover, it is convenient to use units where the magnetic field, M_s , and the magnetic induction are given in Tesla, to connect to the experiment. Then, the Landau-Lifshitz-Gilbert equation has the form:

$$\frac{\partial \mathbf{m}}{\partial t} = -\gamma \mathbf{m} \times \mathbf{H}_{\text{eff}} + \alpha \mathbf{m} \times \frac{\partial \mathbf{m}}{\partial t}, \quad (1)$$

where γ , \mathbf{H}_{eff} , and α are the gyromagnetic ratio, effective magnetic field, and Gilbert damping parameter, respec-

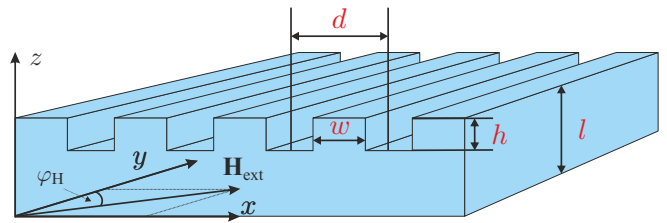


Figure 1. Sketch of the nanograting, the used coordinate system, and the in-plane external magnetic field, \mathbf{H}_{ext} .

tively. For isotropic ferromagnetic materials, the effective magnetic field is given by (see e.g. [51])

$$\mathbf{H}_{\text{eff}} = \mathbf{H}_{\text{ext}} + \mathbf{H}_{\text{d}} + D\nabla^2 \mathbf{m}, \quad (2)$$

where \mathbf{H}_{ext} and \mathbf{H}_{d} are the external and demagnetizing magnetic fields, respectively. The last term in (2) describes the exchange interaction with exchange stiffness constant D , and $\nabla = (\frac{\partial}{\partial x}, \frac{\partial}{\partial y}, \frac{\partial}{\partial z})$.

We stress that both \mathbf{m} and \mathbf{H}_{d} are spatially inhomogeneous and time-dependent quantities. The connection between them is given by the magnetostatic Maxwell equations [51]:

$$\nabla \times \mathbf{H}_{\text{d}} = 0, \quad \nabla \cdot (\mathbf{H}_{\text{d}} + M_s \mathbf{m}) = 0. \quad (3)$$

The described macroscopic quasi-static approach is valid if the magnon wavelength is larger than the atom spacing, and the magnon phase velocities are smaller than the velocity of light [51]. Equations (1)-(3) are the main set of nonlinear differential equations for the NG structure. In addition, we use the standard electrodynamic boundary conditions and free boundary conditions for the magnetization, i.e., $\frac{\partial \mathbf{m}}{\partial \mathbf{n}} = 0$, because this case describes experiments performed on similar structures [25].

Equations (3) are mathematically equivalent to the well-known Maxwell electrostatic equations. Therefore, the general solutions of Eqs. (3) can be found using the Green function for the Laplacian, ∇^2 , (see e.g. [6]). As a result, the demagnetizing field can be written as

$$\mathbf{H}_{\text{d}}(x, z, t) = -\frac{M_s}{2\pi} \nabla \int_{-\infty}^{\infty} dx' \int_0^l \frac{m_x(x-x') + m_z(z-z')}{(x-x')^2 + (z-z')^2} dz'. \quad (4)$$

As one can see from Eq. (4), m_y does not contribute to the demagnetizing field despite that, in general, $m_y \neq 0$. Moreover, the y -coordinate is absent in the integrand, as well. This leads us to the general conclusion that $H_{\text{d},y}$ is zero for any magnetization direction in the NG. Moreover, the demagnetizing field is zero if the magnetization is parallel to the grooves.

The search for the solutions of Eqs. (1)-(3) can be divided into two stages: the steady-state distribution of the magnetization and demagnetizing field and their linear dynamics. In the steady-state, the magnetization, \mathbf{m}^0 , is parallel to $\mathbf{H}_{\text{eff}}^0$ to minimize the free energy of the ferromagnet [51]. In the NG, the spatial distribution of

$\mathbf{H}_{\text{eff}}^0$ is inhomogeneous, as is the spatial distribution of the magnetization (see, e.g., the Eqs. (3)).

For the calculations, we chose polycrystalline Permalloy ($\text{Ni}_{80}\text{Fe}_{20}$) as the NG material. This isotropic ferromagnet possesses very weak magnetostriction, which allows us to exclude from considering the lattice dynamics and consider only magnons. The magnetic parameters [25] for the calculations are the saturation magnetization, $M_s = 0.9236$ T and the exchange stiffness, $D = 23.6$ Tnm². The Gilbert damping parameter α is fixed to zero for the eigenfrequency analysis. A discussion about different materials and parameters can be found in Sec. VI. For the geometrical parameters, we will focus on $d \sim 100$ nm and $l \sim 10$ nm which gives us magnon modes with frequencies ~ 10 GHz and a first-order magnon mode, which is nonuniform in the z -direction (or z -quantized) and shifted to relatively high frequencies.

III. MAGNETIZATION'S STEADY-STATE DISTRIBUTION

The steady-state distribution of the magnetization corresponds to the minimum of the free energy density. In the case of $H_{\text{ext}} = 0$, the magnetization is parallel to the grooves of the NG. In the case of $H_{\text{ext}} \neq 0$, the magnetization in the wires tends to be parallel to the grooves, while the magnetization in the film regions (under the patterned volume) tends to be parallel to \mathbf{H}_{ext} . Thus, the *total* spatial distribution of the steady-state magnetization is non-homogeneous for all directions of \mathbf{H}_{ext} except for $\varphi_H = 0^\circ$.

Let us introduce the quantities $\varphi_M(x, z) = \arctan(m_x^0/m_y^0)$ and $\theta_M(x, z) = \arccos m_z^0$ which are the local azimuthal and polar angles of the magnetization. The deviations of the magnetization direction from the direction of \mathbf{H}_{ext} are given by $\varphi_H - \varphi_M$ and $90^\circ - \theta_M$. The deviations are shown in Fig. 2 for $H_{\text{ext}} = 200$ mT and the following fixed geometrical parameters: $d = 300$ nm, $w = 140$ nm, $h = 13.2$ nm, and $l = 36.8$ nm, which are similar to those in recent experiments [25]. At $\varphi_H = 0$, the magnetization is uniform, hence $\varphi_H - \varphi_M = 0^\circ$ and $90^\circ - \theta_M = 0^\circ$. At $\varphi_H \neq 0$ the azimuthal deviation $\varphi_H - \varphi_M$ reaches its maximum of about 19.8° at $\varphi_H = 65^\circ$. The largest azimuthal deviations are localized at the outer corners of the NG wire. At $\varphi_H = 90^\circ$, the y -component of the magnetization is zero. Thus, the azimuthal deviation is zero. Interestingly, these azimuthal deviations can have both signs. The positive sign means that the magnetization tends to be parallel to the grooves. A small negative azimuthal deviation (up to -3.5°) arises in the region under the grooves, where $H_{d,x}^0$ is positive (see [54] for details). The latter, referred to as a magnetizing field (see, e.g., [25]), slightly rotates the magnetization towards the x -direction, i.e., perpendicular to the grooves.

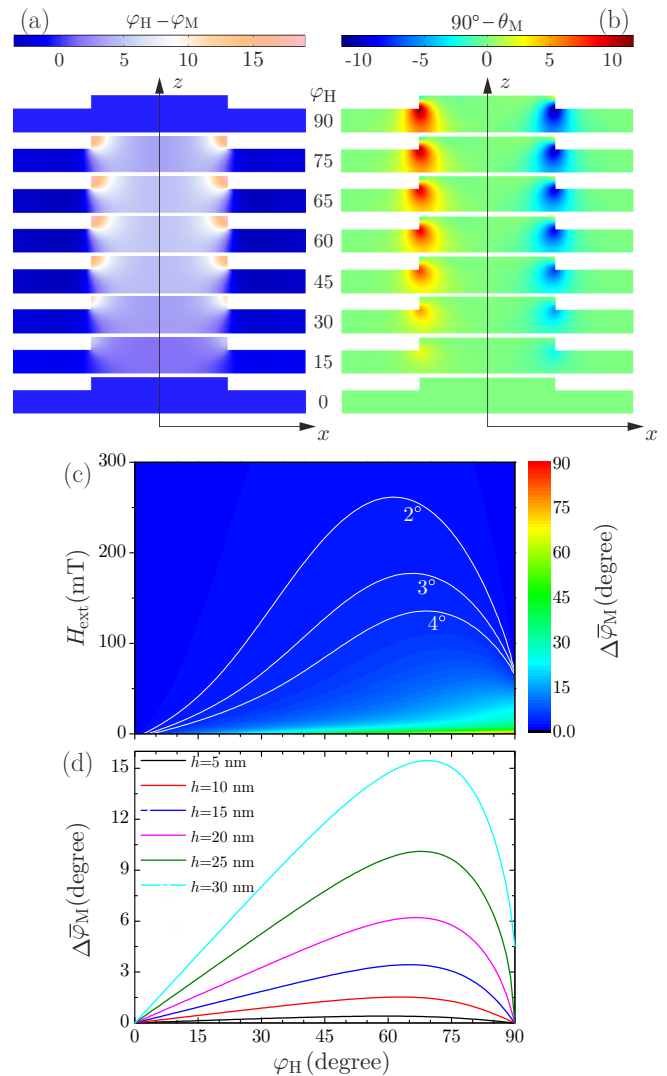


Figure 2. Spatial distributions of (a) $\varphi_H - \varphi_M$ and (b) $90^\circ - \theta_M$ for different directions of \mathbf{H}_{ext} at $H_{\text{ext}} = 200$ mT. The values of φ_H are shown in between (a) and (b). All numbers are given in degrees. (c) Dependencies of the average deviation angle, $\Delta\bar{\varphi}_M$, on φ_H which shows how much the average azimuthal orientation of the magnetization deviates from the \mathbf{H}_{ext} direction, as a function of the direction and strength of \mathbf{H}_{ext} . The white lines represent the contours of constant angles $\Delta\bar{\varphi}_M = 2^\circ, 3^\circ, \text{ and } 4^\circ$. (d) Dependencies of $\Delta\bar{\varphi}_M$ on the direction of \mathbf{H}_{ext} for different depths of the grooves at $H_{\text{ext}} = 200$ mT.

The polar deviation of the magnetization, $90^\circ - \theta_M$, is shown in Fig. 2(b). In this case, the distribution of the polar deviation is an odd function. This is because the symmetry of the polar and azimuthal deviations (or magnetization components) with respect to the center of the NG wire region corresponds to the symmetry of the \mathbf{H}_d^0 components [54]. Note that the positive (negative) polar deviations correspond to positive (negative) m_z^0 . It can be seen that such polar deviations increase with increasing φ_H . The maximum deviation is reached at $\varphi_H = 90^\circ$.

Interestingly, the polar deviations are localized in the inner corners of the NG, while the azimuthal deviations are localized in the outer corners (see Fig 2(a)). This is because the absolute value of the z -component of the demagnetizing field has its maxima at the sharp parts of the NG corners (see [54] for details). For the outer corners, $H_{d,z}^0$ is localized outside the nanograting structure; for the inner corners, it is localized inside the structure and, thereby, rotates the magnetization in the z -direction.

As one can see from the analysis above, the magnetization is not fully saturated (neither homogeneous nor parallel to \mathbf{H}_{ext}) even at $H_{\text{ext}} = 200$ mT, which is strong enough for saturation of a plain Permalloy film. Due to the demagnetizing field, the magnetization in the NG saturates asymptotically with increase of the external magnetic field strength. For example, at $H_{\text{ext}} = 10$ T and $\varphi_H = 90^\circ$, the polar deviation, $90^\circ - \theta_M$, changes from -1.5° to 1.5° . However, the magnetization deviates considerably from the external magnetic field direction only at the corners of the NG. Therefore, for practical purposes, it is convenient to introduce the *average azimuthal angle* of the magnetization, $\bar{\varphi}_M = \int \varphi_M dV$, which describes the average orientation of the magnetization. Here dV is the unit volume element. In addition, let us introduce the average deviation angle, $\Delta\bar{\varphi}_M = \varphi_H - \bar{\varphi}_M$, which describes how much the average azimuthal orientation of the magnetization deviates from the \mathbf{H}_{ext} direction. The magnetization can be considered saturated on average if $\sin \Delta\bar{\varphi}_M \ll 1$.

Figure 2(c) shows the dependencies of $\Delta\bar{\varphi}_M$ on different magnetic field directions and strengths. The meaning of the white contours in Fig. 2(c) is that for any magnetic field direction and strength above a contour $\Delta\bar{\varphi}_M = \text{const}$, the values of $\Delta\bar{\varphi}_M < \text{const}$. For instance, at $H_{\text{ext}} = 200$ mT, $\Delta\bar{\varphi}_M$ is less than 3° at any magnetic field direction.

Figure 2(d) shows the dependencies of $\Delta\bar{\varphi}_M$ on the external magnetic field direction for different depths of the grooves, h , calculated at $H_{\text{ext}} = 200$ mT. The maximum position slightly shifts toward higher φ_H from 60° for the shallow NG ($h = 5$ nm) to 69° for the deep NG ($h = 30$ nm). The reason why $\Delta\bar{\varphi}_M$ demonstrates a slow increase at $\varphi_H \lesssim 50^\circ$ and a rapid decrease at $\varphi_H \gtrsim 75^\circ$ is due to the collective dipole-dipole interaction. That is, the spatial region, where the magnetization direction is close to the field direction grows with increasing H_{ext} . At φ_H , which gives the maximum of $\Delta\bar{\varphi}_M$, this region becomes large enough to change the direction of the magnetization in the wire region of the NG. Then, the magnetization in this region attracts the magnetization at the corners of the NG leading to the rapid decrease of m_y . As a result, $\Delta\bar{\varphi}_M$ drops sharply to zero at $\varphi_H = 90^\circ$. Note, that for the NG with $h = 30$ nm, one must apply much larger magnetic fields than $H_{\text{ext}} = 200$ mT to saturate the magnetization for any φ_H .

Keeping this physical picture in mind, we can turn to the analysis of magnons in the NG.

IV. CLASSIFICATION OF THE MAGNON EIGENMODES

The magnetic dynamics of a ferromagnet consists of the spatially inhomogeneous precession of the magnetization around $\mathbf{H}_{\text{eff}}^0$. This time- and space-dependent precessional motion can be considered as a superposition of the magnon eigenmodes of the NG. To describe it, we have linearized the main set of equations by introducing a dynamic magnetization, $\delta\mathbf{m}$, with $\delta m \ll m^0$, and a dynamic demagnetizing field, $\delta\mathbf{H}_d$, with $\delta H_d \ll M_s$. In order to calculate the dispersion curves and spatial profiles of the magnon modes, we performed an eigenfrequency analysis with Floquet-Bloch periodic boundary conditions, i. e. $\mathbf{u}_d = \mathbf{u}_s \exp(-ik_x d)$, where k_x is the Bloch wavenumber, and \mathbf{u}_d as well as \mathbf{u}_s are dependent variables at the destination and source boundaries, respectively.

The solutions of the eigenfrequency problem give the spatially inhomogeneous complex-valued Fourier components of the dynamic magnetization and demagnetizing field. For the characterization of the magnon modes' spatial profiles, let us choose the z -component of the dynamic magnetization because it is nonzero for any in-plane \mathbf{H}_{ext} . Below, we focus on the spatial profiles, which correspond to *the center* of the Brillouin zone, i.e., $k_x = 0$. The real-valued solution for δm_z in the time domain can be expressed in the form $\delta m_z = |\delta m_{z,\omega}| \cos(\omega t + \phi_z)$, where ω is the magnon angular frequency, $\delta m_{z,\omega}$ is the Fourier component of δm_z , and $\phi_z = \text{atan2}(\text{Im}(\delta m_{z,\omega}), \text{Re}(\delta m_{z,\omega}))$ is the phase. The latter is spatially inhomogeneous. Thus, the magnon modes' spatial profiles change during propagation [25]. Moreover, the difference between the supremum and infimum values of δm_z , $\mathcal{D}_m(t) = \sup(\delta m_z) - \inf(\delta m_z)$, varies with time. However, we found that at the time, which corresponds to the maximum of $\mathcal{D}_m(t)$, each mode profile becomes purely symmetric or antisymmetric with respect to the center of the NG wire region. This time can be found as $t = (\tau_s - \phi_{z,c})/\omega$, where $\tau_s = s\pi$ for symmetric modes (s is an integer number), $\tau_s = s\pi/2$ for antisymmetric modes, and $\phi_{z,c}$ is the value of the phase at the center of the unit cell of the NG ($x = 0, z = l/2$ in our coordinate system). Thus, we use the symmetry at this time for characterizing a magnon mode. This symmetry determines the possibility of the mode being excited by a spatially homogeneous excitation (the laser pulse or the uniform ac- magnetic field in a FMR experiment).

According to the Floquet-Bloch theorem, each eigenmode contains an infinite number of wave vectors $q_x = k_x + n \frac{2\pi}{d}$, where n is an integer number. To characterize the magnon modes by the number, n , we perform the spatial Fourier transform

$$\delta m_{z,n} = \int \delta m_z(x, z) \exp\left(in \frac{2\pi}{d} x\right) \exp(iq_z z) dV \quad (5)$$

and find the set of n , which dominate in each eigenmode. Here q_z is the z -component of the wavevector. Further

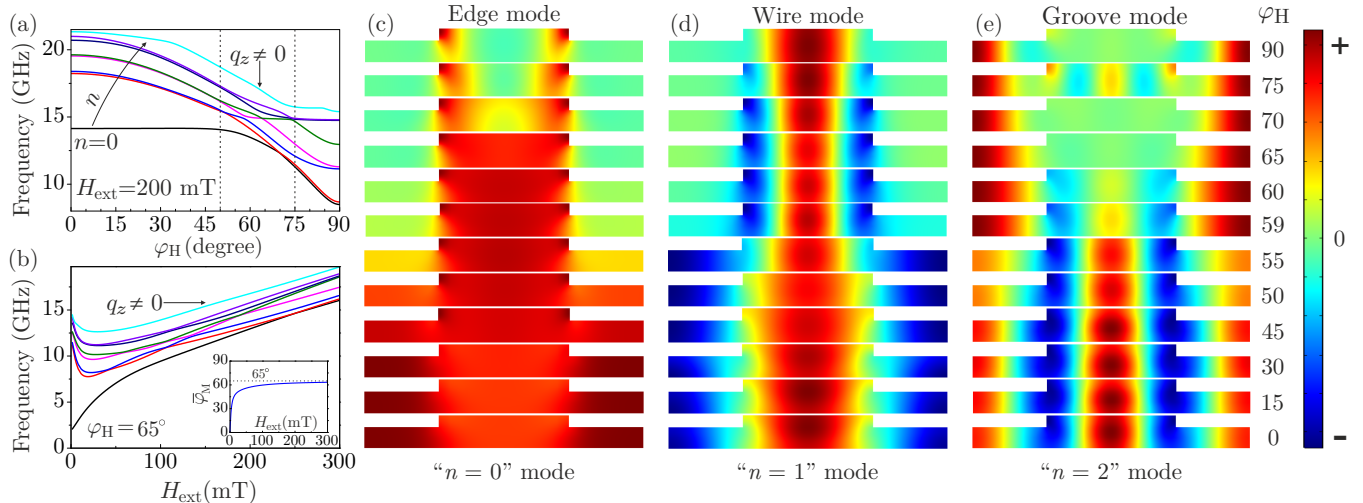


Figure 3. Magnetic field direction (a) and strength (b) dependencies of magnon frequencies. The arrow shows the direction of the number n increase at $\varphi_H \lesssim 50^\circ$: the ground magnon branch with $n = 0$ and the three next pairs with, $n = 1, 2$, and 3 , respectively. The vertical dashed lines indicate the transition range. The inset in (b) shows the magnetic field dependence of the average azimuthal angle of the magnetization, $\bar{\varphi}_M$. (c)-(e) Evolutions of the main symmetric magnon modes under rotation of the magnetic field. The values of φ_H are given in degrees. All quantities here correspond to the center of the Brillouin zone ($k_x = 0$) and $H_{\text{ext}} = 200$ mT.

we will focus on the quasiuniform eigenmodes in the z direction and put $q_z = 0$.

The result of an eigenfrequency analysis is presented in Fig. 3(a), which shows the angle dependence of the magnon frequencies, $\omega/2\pi$ at $H_{\text{ext}} = 200$ mT. Here, one can observe a complicated non-monotonic behavior with magnon-magnon interaction and corresponding avoided crossings of the interacting modes at the intersections. Despite that, the general tendency is typical for ferromagnets (see, for instance, [48, 49]): the magnon frequency decreases with changing of the direction of \mathbf{H}_{ext} from the easy axis ($\varphi_H = 0^\circ$) to the hard axis ($\varphi_H = 90^\circ$). Interestingly, the frequency of the ground magnon mode does not significantly depend on the direction of \mathbf{H}_{ext} for $\varphi_H \lesssim 50^\circ$ and can be estimated with reasonable accuracy using the Kittel formula [13].

Figure 3(b) shows the magnetic field dependence of the magnon frequencies at $\varphi_H = 65^\circ$. The ground magnon branch (black line) demonstrates a simple Kittel-like behavior. All following branches firstly decrease and, then, increase in their frequencies with increasing external magnetic field strength. The turning point at $H_{\text{ext}} \approx 15$ mT corresponds to the field strength overcoming the anisotropy field when the steady-state magnetization turns toward \mathbf{H}_{ext} . This is illustrated in the inset, which shows the magnetic field dependence of the average azimuthal angle of the magnetization, $\bar{\varphi}_M(H_{\text{ext}})$, for the chosen φ_H .

The spatial profiles of the magnon modes in the DE and BV geometries can be found in [25] and [54]. For the DE geometry, the magnon modes (quasiuniform in the z direction) can be completely characterized by the single spatial harmonic along the x -axis, characterized by the number n . The ground quasiuniform magnon mode

corresponds to $n = 0$, and the next pair of antisymmetric and symmetric modes have $n = 1$ (see the amplitudes of the spatial Fourier transform, $|\delta m_{z,n}|$, in [54]), etc. In the BV geometry, the localization of magnon modes is fragmented into separate regions of wires and grooves. As a result, each magnon mode consists of several dominant n [55]. For example, the ground symmetric edge mode possesses three dominant n : $n = 3, 2, 0$ (hereafter, the sequence is given in descending order of $|\delta m_{z,n}|$, see [54]). The symmetric wire mode can be characterized by $n = 1, 0, 2$, and the symmetric groove mode by $n = 2, 0, 1$.

Figures 3(c)-(e) show the evolution of the spatial profiles of the three lowest symmetric magnon modes under rotation of the magnetic field. One can see that the ground quasiuniform (Kittel) mode ($n = 0$) in the DE geometry evolves to the edge mode in the BV geometry. The magnon modes with $n = 1$ and $n = 2$ evolve to wire and groove modes, respectively. Note that we add the field direction $\varphi_H = 59^\circ$ to show the smooth transition of the $n = 2$ mode to the groove mode. One can see that for the field directions up to $\approx 50^\circ$, the magnon modes can be considered DE-like, because their spatial profiles maintain their distributions and can be characterized by the single number n . Similarly, starting from $\varphi_H \approx 75^\circ$ and up to 90° , the magnon modes can be considered BV-like. For the range $50^\circ - 75^\circ$, the magnon modes' profiles considerably differ from DE-like and BV-like modes. We call these modes *transition magnon modes*. Note that the spatial modulation in the wire region of the groove mode at $\varphi_H = 75^\circ$ is due to coupling with the higher order wire magnon mode (similar to the 5-th mode in Fig. S6(d) in [54]).

Figures 3(c)-(e) clearly show that the intermediate di-

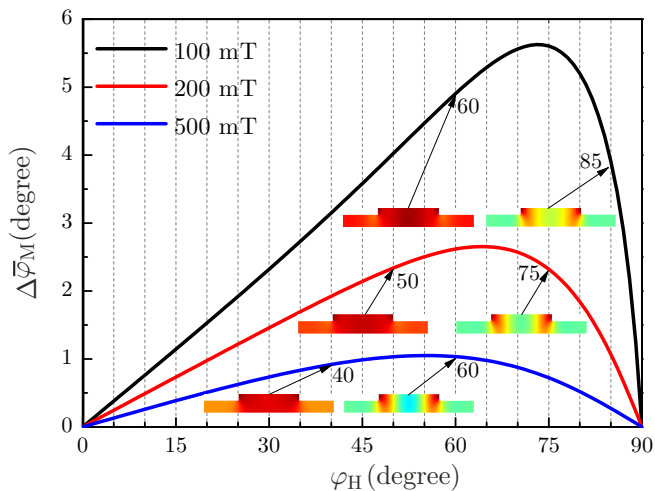


Figure 4. Magnetic field direction dependence of $\Delta\bar{\varphi}_M$, showing the transition from DE-like modes to BV-like modes for three different values of H_{ext} .

rections of \mathbf{H}_{ext} can be used for adjusting the spatial overlap of the selected magnon mode with another periodic excitation, such as an elastic wave, to maximize the magneto-elastic coupling strength [35–37, 56, 57]. In the latter case, the magneto-elastic interaction can occur between symmetric magnon and symmetric phonon modes, as well as between symmetric magnon modes and antisymmetric phonon modes [37] or in other combinations [35, 36].

Notably, the transition range is defined by the steady-state magnetization distribution in the NG. From the analysis of the previous section and, in particular, from Fig. 2, one can see that the transition range is located around the maximum of $\Delta\bar{\varphi}_M$. We stress that the low-order magnon modes are influenced by the static demagnetizing fields more strongly than the high-order modes because the wavelengths of the high-order modes are smaller than the NG period. Figure 4 shows how the transition range depends on the external magnetic field strength: the maximum of $\Delta\bar{\varphi}_M$ shifts towards its asymptotic limit of 45° with increasing H_{ext} . In particular, for $\varphi_H = 60^\circ$, the ground symmetric magnon mode is still the quasiuniform mode at $H_{\text{ext}} = 100$ mT, but becomes already the edge mode at $H_{\text{ext}} = 500$ mT. The position of the transition range depends on the interplay of the external magnetic field and the demagnetizing field. The transition range width decreases with the increasing field strength. For commonly used magnetic fields (~ 100 mT), the modes are DE-like at $\varphi_H \leq 45^\circ$. The existence of the transition magnon modes in the transition range of the magnetic field directions with their relation to the static NG magnetization is one of the main results of the paper.

Spatial profiles of transition magnon modes are shown in Fig. 5 for $\varphi_H = 65^\circ$ and two different depths of the grooves. A distinctive feature of these modes is that they are well distributed in separate parts of the NG.

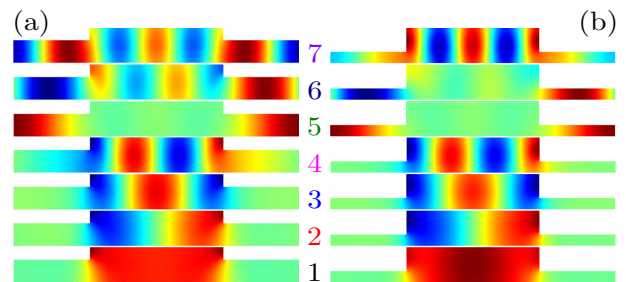


Figure 5. Spatial distributions of transition magnon modes for two depths of the grooves: $h = 13.2$ nm and $h = 25$ nm. The colors of sequence numbers correspond to the line colors in Fig. 3(a), (b), and the color scale is the same as in Fig. 3(c)-(e).

For example, the ground transition mode, which transforms from the uniform to the edge mode, is localized in the wire region. However, in contrast to the edge mode, it has there a quasiuniform distribution (see Fig 3(c)). This mode is also different from the wire mode because it has a significantly different spatial spectrum given by $n = 0, 1, 3$, while for the wire mode $n = 1, 0, 2$ (see Fig. S4 in [54]). All four lowest magnon modes are localized in the wire region, and their sequence number indicates the number of peaks in the wire region. Then come the symmetric and antisymmetric transition modes localized in the grooves, but with a broader spatial distribution than the groove mode in the BV geometry. The following modes of higher orders, as well as the high-order modes in the DE and BV geometries, are weakly influenced by the demagnetizing field because their wavelengths are smaller than the NG period. The spatial profiles of transition magnon modes weakly depend on the depth of the grooves.

V. MAGNON DISPERSION AND NONRECIPROCALITY

The dispersion is another crucial characteristic of magnons that gives the wave vector dependencies of the magnon modes' frequencies and their group velocities, as well as the spectral positions and widths of the magnon band gaps. It can be directly measured by Brillouin light scattering techniques [2, 7–9, 42] and determines the transient signals in the magneto-optical pump-probe experiments with microscopic resolution.

Figures 6 (a)-(h) show the evolution of the magnon dispersions under rotation of the magnetic field from $\varphi_H = 0^\circ$ to $\varphi_H = 90^\circ$ at $H_{\text{ext}} = 200$ mT. The nonreciprocity and indirect band gaps can be observed for all directions of \mathbf{H}_{ext} except $\varphi_H = 90^\circ$. With increasing φ_H , the magnon dispersion branches shift to lower frequencies and several low-lying branches become flat. Due to the vanishingly small dynamic demagnetizing field of the ground DE-like branch, it can be qualitatively described

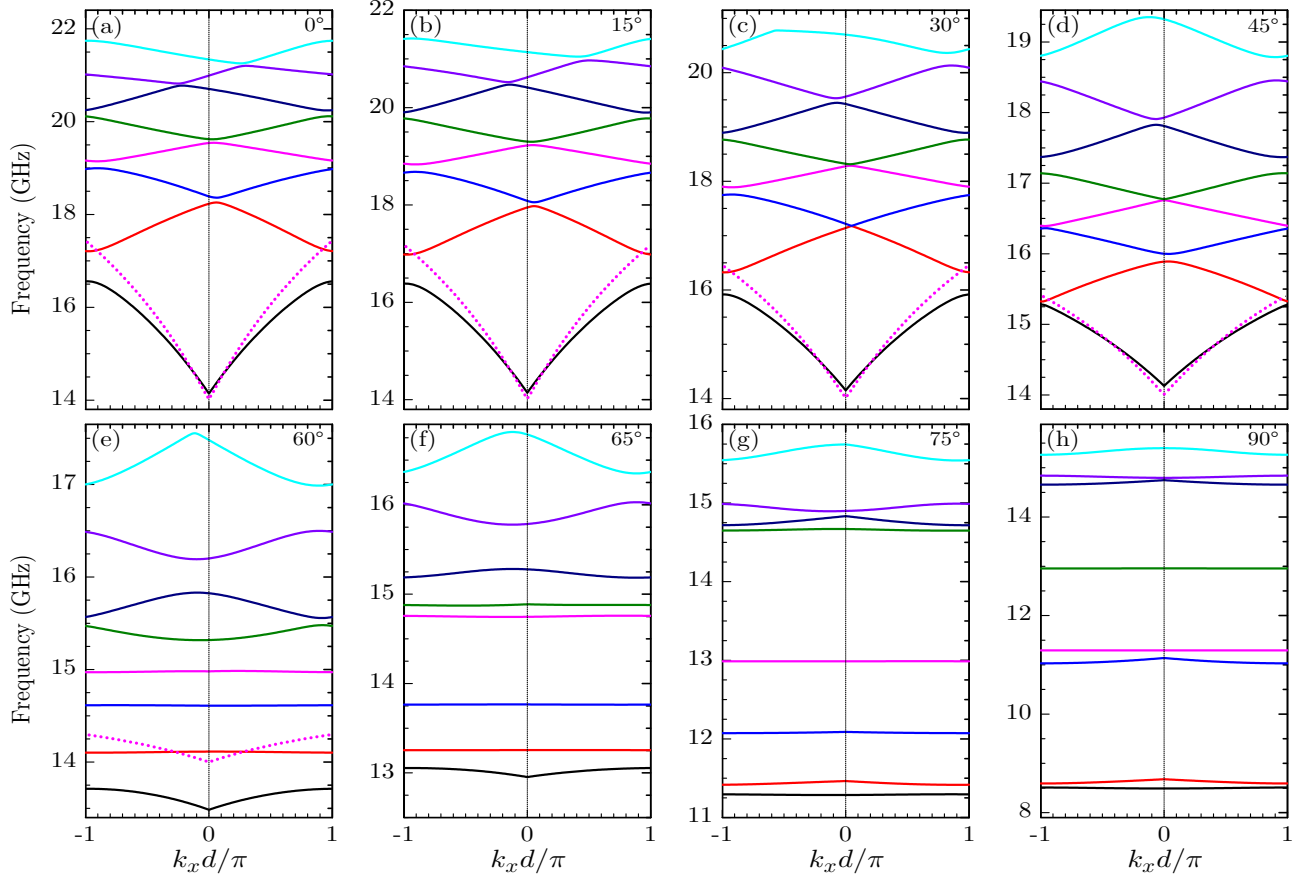


Figure 6. (a)-(h) Magnon dispersion evolution under rotation of \mathbf{H}_{ext} from $\varphi_H = 0^\circ$ (DE) to $\varphi_H = 90^\circ$ (BV) at $H_{\text{ext}} = 200$ mT. The values of φ_H are shown in the right upper corners. Note that the vertical scales are different in (a)-(h). The pink dotted lines represent the corresponding thin film dispersions (see Eq. (6)).

by the thin-film dispersion [58, 59]:

$$\omega^2 = \gamma \left(H_{\text{ext}} + M_s \left(1 - \frac{1 - e^{-q_x l}}{q_x l} \right) \cos^2 \varphi_H + Dq_x^2 \right),$$

$$\times \gamma \left(H_{\text{ext}} + M_s \left(\frac{1 - e^{-q_x l}}{q_x l} \right) + Dq_x^2 \right), \quad (6)$$

in the range of magnetic field directions before the transition range, i.e., at $\varphi_H \lesssim 50^\circ$. This dispersion is shown by dots in Fig. 6(a)-(e) in the first Brillouin zone. At $\varphi_H = 0^\circ$, the seven lowest branches originate from the Eq. (6) due to the folding of the dispersion curves. Then comes the z -quantized branch #8, which starts its own series of high frequency folded dispersion curves. The agreement between the numerical solutions and Eq.(6) becomes unfulfilled in the transition range and the range of BV-like modes for the chosen set of parameters because of relatively strong demagnetizing fields. Therefore, a better agreement can be reached if $q_x l \ll 1$ and $h/l \ll 1$. Note, that in the geometry close to BV the dispersions of several lowest branches are flat [24] already at $h = 5$ nm (all other parameters are fixed as in Sec. II).

A fundamental characteristic of the dispersion curves is the nonreciprocity, i.e., $\omega(k_x) \neq \omega(-k_x)$. The nonreciprocity in the NG arises from the symmetry of the

structure and the dynamical demagnetizing fields. In the DE geometry, both δm_x and δm_z contribute equally to $\delta \mathbf{H}_d$ (see Eq. (4)). As a result, at a random time, $\delta \mathbf{H}_d$ is neither symmetric nor antisymmetric, which causes the propagating behavior of the modes. In the BV geometry, $\delta \mathbf{H}_d$ is defined by δm_z . As a result, the parity of the modes is conserved at any time and the dispersion is reciprocal.

One may note, that the slopes of the dispersion curves depend on φ_H non-monotonically. To show this explicitly, we calculated the group velocities $v_g = \frac{d\omega}{dk_x}$ at the center of the Brillouin zone and at two fixed values of the Bloch wavevector $k_x d / \pi = \pm 0.2$. The dependencies of $v_g(\varphi_H)$ for the seven lowest magnon modes are shown in Fig. 7. First, let us consider the case $k_x = 0$. The group velocity of the ground quasiform magnon mode #1 is close to zero (Fig. 7(a)). This is due to the vanishingly small dynamic demagnetizing fields that the quasiform mode creates. Consequently, this mode is reciprocal and has vanishingly small v_g at $k_x = 0$. The next pairs, namely #2 and #3, #4 and #5, #6 and #7, possess similar dependencies with opposite signs. For $\varphi_H = 90^\circ$, the group velocities for all modes are zero. Note that the highest magnon group velocity is observed not for the

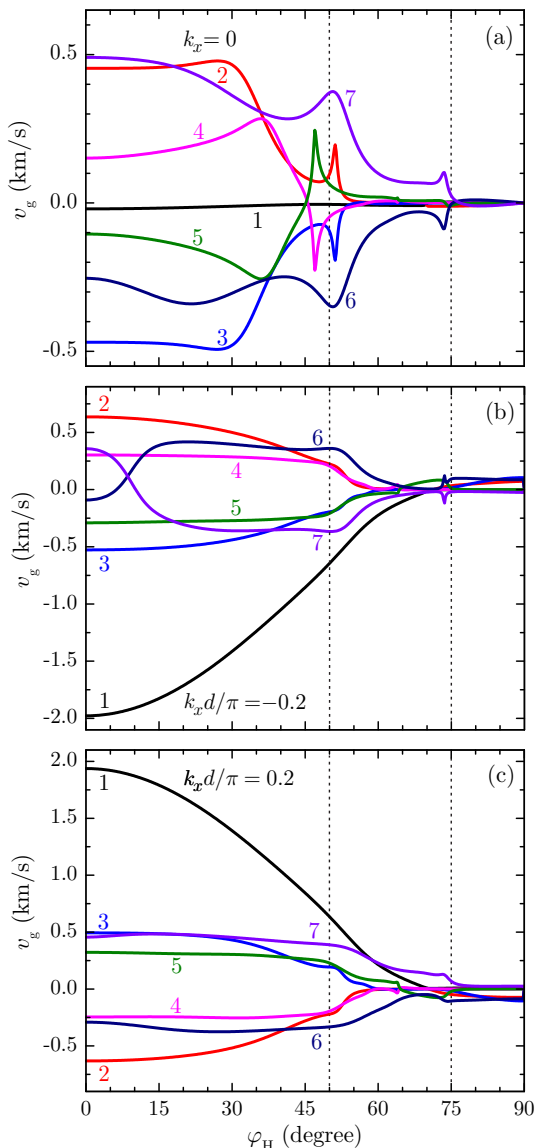


Figure 7. Group velocities of the seven lowest magnon modes for $k_x = 0$ (a), $k_x d / \pi = -0.2$ (b) and $k_x d / \pi = 0.2$ (c). The vertical dashed lines indicate the transition range.

DE geometry. The magnon mode #3 with $n = 1$ reaches $v_g \approx -0.5$ km/s around $\varphi_H = 30^\circ$. The group velocities of modes #2 – 7 rapidly decrease at the angles $\varphi_H \gtrsim 50^\circ$, which corresponds to the transition range. Thus, the group velocities of transition modes are close to zero. The lower magnon modes are more strongly influenced by the static demagnetizing fields than the higher-order modes, as the wavelength of these modes is smaller than the NG period. Therefore, the group velocities of high order modes are nonzero up to $\varphi_H = 90^\circ$.

At $k_x \neq 0$, the fastest magnon mode is the ground one in the DE geometry with $|v_g| \approx 2$ km/s. The pairs #2 and #3, #4 and #5, #6 and #7, possess similar dependencies with opposite signs as in the case $k_x = 0$. The

velocities of transition modes are close to zero due to the flattening of the dispersions. Interestingly, the indirect band gap between the #6 and #7 modes at $\varphi_H \approx 10^\circ$ causes the strong dependence of the group velocity on the magnon propagation direction: the group velocity of mode #7 changes from zero to 0.5 km/s for negative and positive propagation directions, respectively.

VI. VALIDITY AND APPLICATIONS

Finally, let us discuss the validity and generality of the obtained numerical results. The validity of our approach was successfully proven by solving standard micromagnetic problems [54, 60]. Our results are valid for relatively thin NGs, i.e. if the z -quantized magnon branch is well above the ground magnon branch. We found numerically that both the magnon dispersions and spatial profiles remain qualitatively similar for surface modulated magnonic crystals with parameters that satisfy the criterion: $l_e d / l^2 > c_0$, where $l_e = \sqrt{D / M_s}$ is the exchange length, and $c_0 \approx 1$. For the parameters used in the paper, $l_e d / l^2 \approx 1.1$ which is close to the lower limit of $l_e d / l^2$. The exchange length is of the same order for most common ferromagnetic metals. For example, for CoFeB: $l_e \approx 4.7$ nm (see e.g. [61]), for permalloy: $l_e \approx 5.1$ nm, for nickel: $l_e \approx 7.7$ nm (see e.g. [62]), and for cobalt: $l_e \approx 8.1$ nm (see e.g. [63]). For such materials as CoFe: $l_e \approx 3.2$ (see e.g. [64]) and for FeGa: $l_e \approx 4.1$ nm (see e.g. [65]), the above criterion is violated for $l > 30$ nm. For the mentioned dielectric ferromagnet YIG, the exchange length is larger than in metals: $l_e \approx 17.6$ nm (see [66]). Note, that in addition to the mentioned criterion, the magnon characteristics can be considerably different for the extremal geometrical parameters. For instance, the edge mode does not exist if $h / l \rightarrow 0$ and the groove mode, obviously, does not exist in full magnonic crystals ($h \approx l$). In the case $l_e d / l^2 < 1$, the transition region is existent as far as demagnetizing fields exist. It is located also between $\varphi_H = 45^\circ$ and 90° . However, with increasing film thickness, the slope of the ground Kittel-like magnon branch increases and the z -quantized branch downshifts. Therefore, eventually, these branches intersect and the corresponding magnon mode characteristics become considerably modified due to strong magnon-magnon coupling which causes a band structure renormalization. The detailed description of this case is beyond the scope of this paper.

The presence of the transition magnon modes with complex characteristics is important for experimental studies and technological applications based on the excitation and detection of coherent magnons by ultrashort laser pulses. Such investigations are typically implemented for intermediate directions of the external magnetic field. The choice of the experimental geometry is determined by the mechanism of excitation: ultrafast thermal- and/or strain- (excited by thermal stress) induced modulations of the magnetic anisotropy, which are

the most effective at the intermediate directions of \mathbf{H}_{ext} . The coherent magnon response in NG is a superposition of the excited magnon modes. The excitation efficiency of a certain mode is determined by its spatial overlap with the optically induced impact [35, 46, 48]. Control of the spatial profiles of the magnon modes by the direction and/or strength of the external magnetic field allows tuning of the spatial distribution and frequency spectrum of the coherent magnon response. This approach can be especially effective in a NG with enhanced magneto-elastic interaction, in which the excitation of coherent magnons is mediated by optically excited phonon eigenmodes of the NG [33, 37]. The interaction of specific phonon and magnon eigenmodes can be fully suppressed in the case of poor spatial matching, or enhanced up to formation of a hybridized state in the case of perfectly matched modes [37, 57]. This tunability is important for hybrid magnonics [67, 68] with potential quantum applications.

Optical excitation of the propagating spin waves is another possible experimental route [49, 69, 70], which can utilize the tunability of transition magnon modes. Non-reciprocity of the magnon modes makes possible the excitation of propagating spin waves even in the case of uniform optical excitation. However, the magnon group velocities at intermediate directions are pretty low for the considered geometrical/material parameters. The typical value of the Gilbert damping for Permalloy is $\alpha = 0.01$ which corresponds to a magnon lifetime of ~ 1 ns. In this case, the propagation length of a magnon mode with $v_g = 0.5$ km/s is ~ 500 nm, which is comparable with the NG period. To increase the propagation distance, one can use materials with weak damping, e.g. yttrium-iron-garnet (YIG) or $\text{Co}_{0.25}\text{Fe}_{0.75}$ with comparable Gilbert damping $\sim 10^{-4}$ [18, 71]. The group velocities also increase with increasing ferromagnet film thickness [72]. For example, our calculations give $v_g > 15$ km/s for the ground magnon mode near the center of the Brillouin

zone in case of $l = 200$ nm (all other parameters taken the same as in Sec. II).

VII. CONCLUSION

To conclude, we have investigated the magnon modes of ferromagnetic nanogratings at intermediate in-plane directions of the external magnetic field that were not addressed so far. We have used COMSOL Multiphysics to calculate the magnon dispersions, spatial profiles, and their dependencies on the direction and strength of the external magnetic field. We have found a transition range of magnetic fields with a width of $\sim 25^\circ$ where the magnon characteristics are very different from the characteristics in the widely investigated Damon-Eshbach and Backward Volume geometries. The range width and its position depend on the interplay of the external magnetic field and the static demagnetizing field. The modes in the transition range are slowly propagating waves that are well separated in certain parts of the NG because of their unique combinations of spatial Fourier harmonics. We have shown that by changing the magnetic field direction around the transition range, one can switch between three different types of magnon modes and choose the magnon modes of desirable characteristics.

VIII. ACKNOWLEDGEMENTS

We acknowledge the late B. A. Glavin for his valuable contribution to this work. We are thankful to Tetiana Linnik and Oksana Chubykalo-Fesenko for fruitful discussions. The work was supported by the Bundesministerium für Bildung und Forschung through the project VIP+ "Nanomagneton" and by the Volkswagen Foundation (grant no. 97758).

-
- [1] B. Lenk, H. Ulrichs, F. Garbs, and M. Münzenberg, The building blocks of magnonics, *Phys. Rep.* **507**, 107 (2011).
 - [2] M. Krawczyk and D. D Grundler, Review and prospects of magnonic crystals and devices with reprogrammable band structure, *J. Phys.: Condens. Matter* **26**, 123202 (2014).
 - [3] A. V. Chumak, V. I. Vasyuchka, A. A. Serga, and B. Hillebrands, Magnon spintronics, *Nat. Phys.* **11**, 453 (2015).
 - [4] S. A. Nikitov, P. Tailhades, and C. S. Tsai, Spin waves in periodic magnetic structures – magnonic crystals, *J. Magn. Magn. Mater.* **236**, 320 (2001).
 - [5] M. P. Kostylev, A. A. Stashkevich, and N. A. Sergeeva, Collective magnetostatic modes on a one-dimensional array of ferromagnetic stripes, *Phys. Rev. B* **69**, 064408 (2004).
 - [6] K. Y. Guslienko and A. N. Slavin, Boundary conditions for magnetization in magnetic nanoelements, *Phys. Rev. B* **72**, 014463 (2005).
 - [7] G. Gubbiotti, S. Tacchi, G. Carlotti, P. Vavassori, N. Singh, S. Goolaup, A. O. Adeyeye, A. Stashkevich, and M. Kostylev, Magnetostatic interaction in arrays of nanometric permalloy wires: A magneto-optic kerr effect and a brillouin light scattering study, *Phys. Rev. B* **72**, 224413 (2005).
 - [8] G. Gubbiotti, S. Tacchi, G. Carlotti, N. Singh, S. Goolaup, A. O. Adeyeye, and M. Kostylev, Collective spin modes in monodimensional magnonic crystals consisting of dipolarly coupled nanowires, *Appl. Phys. Lett.* **90**, 092503 (2007).
 - [9] M. Kostylev, P. Schrader, R. L. Stamps, G. Gubbiotti, G. Carlotti, A. O. Adeyeye, S. Goolaup, and N. Singh, Partial frequency band gap in one-dimensional magnonic crystals, *Appl. Phys. Lett.* **92**, 132504 (2008).
 - [10] N. I. Polushkin, Excitation of coupled oscillations in lateral ferromagnetic heterostructures, *Phys. Rev. B* **77**, 180401(R) (2008).

- [11] M. Mruczkiewicz, M. Krawczyk, V. K. Sakharov, Y. V. Khivintsev, Y. A. Filimonov, and S. A. Nikitov, Standing spin waves in magnonic crystals, *J. Appl. Phys.* **113**, 093908 (2013).
- [12] M. Mruczkiewicz, M. Krawczyk, G. Gubbiotti, S. Tacchi, Y. A. Filimonov, D. V. Kalyabin, I. V. Lisenkov, and S. A. Nikitov, Nonreciprocity of spin waves in metallized magnonic crystal, *New J. Phys.* **15**, 113023 (2013).
- [13] I. Lisenkov, D. Kalyabin, S. Osokin, J. W. Klos, M. Krawczyk, and S. Nikitov, Nonreciprocity of edge modes in 1d magnonic crystal, *J. Magn. Magn. Mater.* **378**, 313 (2015).
- [14] J. Rychly, P. Gruszecki, M. Mruczkiewicz, J. W. Klos, S. Mamica, and M. Krawczyk, Magnonic crystals – prospective structures for shaping spin waves in nanoscale, *Low Temperature Physics* **41**, 745 (2015).
- [15] A. V. Chumak, A. A. Serga, B. Hillebrands, and M. P. Kostylev, Scattering of backward spin waves in a one-dimensional magnonic crystal, *Appl. Phys. Lett.* **93**, 022508 (2008).
- [16] A. V. Chumak, A. A. Serga, S. Wolff, B. Hillebrands, and M. P. Kostylev, Design and optimization of one-dimensional ferrite-film based magnonic crystals, *J. Appl. Phys.* **105**, 083906 (2009).
- [17] A. V. Chumak, A. A. Serga, S. Wolff, B. Hillebrands, and M. P. Kostylev, Scattering of surface and volume spin waves in a magnonic crystal, *Appl. Phys. Lett.* **94**, 172511 (2009).
- [18] A. A. Serga, A. V. Chumak, and B. Hillebrands, YIG magnonics, *J. Phys. D: Appl. Phys.* **43**, 264002 (2010).
- [19] P. Landeros and D. L. Mills, Spin waves in periodically perturbed films, *Phys. Rev. B* **85**, 054424 (2012).
- [20] G. N. Kakazei, X. M. Liu, J. Ding, and A. O. Adeyeye, Ni80fe20 film with periodically modulated thickness as a reconfigurable one-dimensional magnonic crystal, *Appl. Phys. Lett.* **104**, 042403 (2014).
- [21] G. R. Aranda, G. N. Kakazei, J. González, and K. Y. Guslienko, Ferromagnetic resonance micromagnetic studies in patterned permalloy thin films and stripes, *J. Appl. Phys.* **116**, 093908 (2014).
- [22] V. D. Bessonov, M. Mruczkiewicz, R. Gieniusz, U. Guzowska, A. Maziewski, A. I. Stognij, and M. Krawczyk, Magnonic band gaps in yig-based one-dimensional magnonic crystals: An array of grooves versus an array of metallic stripes, *Phys. Rev. B* **91**, 104421 (2015).
- [23] M. Langer, F. Röder, R. A. Gallardo, T. Schneider, S. Stienen, C. Gatel, R. Hübner, L. Bischoff, K. Lenz, J. Lindner, P. Landeros, and J. Fassbender, Role of internal demagnetizing field for the dynamics of a surface-modulated magnonic crystal, *Phys. Rev. B* **95**, 184405 (2017).
- [24] R. A. Gallardo, T. Schneider, A. Roldán-Molina, M. Langer, J. Fassbender, K. Lenz, J. Lindner, and P. Landeros, Dipolar interaction induced band gaps and flat modes in surface-modulated magnonic crystals, *Phys. Rev. B* **97**, 144405 (2018).
- [25] M. Langer, R. A. Gallardo, T. Schneider, S. Stienen, A. Roldán-Molina, Y. Yuan, K. Lenz, J. Lindner, P. Landeros, and J. Fassbender, Spin-wave modes in transition from a thin film to a full magnonic crystal, *Phys. Rev. B* **99**, 024426 (2019).
- [26] R. A. Gallardo, D. Cortés-Ortuño, T. Schneider, A. Roldán-Molina, F. Ma, R. E. Troncoso, K. Lenz, H. Fangohr, J. Lindner, and P. Landeros, Flat bands, indirect gaps, and unconventional spin-wave behavior induced by a periodic dzyaloshinskii-moriya interaction, *Phys. Rev. Lett.* **122**, 067204 (2019).
- [27] A. V. Chumak, A. A. Serga, and B. Hillebrands, Magnon transistor for all-magnon data processing, *Nat. Comm.* **5**, 4700 (2014).
- [28] A. Khitun, M. Bao, and K. L. Wang, Magnonic logic circuits, *J. Phys. D: Appl. Phys.* **43**, 264005 (2010).
- [29] K. Vogt, F. Y. Fradin, J. E. Pearson, T. Sebastian, S. D. Bader, B. Hillebrands, and H. Hoffmann, A. Schultheiss, Realization of a spin-wave multiplexer, *Nat. Comm.* **5**, 3727 (2014).
- [30] M. Balinskiy, H. Chiang, and K. A., Realization of spin wave switch for data processing, *AIP Adv.* **8**, 056628 (2018).
- [31] S.-K. Kim, K.-S. Lee, and D.-S. Han, A gigahertz-range spin-wave filter composed of width-modulated nanostrip magnonic-crystal waveguides, *Appl. Phys. Lett.* **95**, 082507 (2009).
- [32] H. Yu, G. Duerr, R. Huber, M. Bahr, T. Schwarze, F. Brandl, and D. Grundler, Omnidirectional spin-wave nanograting coupler, *Nat. Comm.* **4**, 2702 (2013).
- [33] A. S. Salasyuk, A. V. Rudkovskaya, A. P. Danilov, B. A. Glavin, S. M. Kukhtaruk, M. Wang, A. W. Rushforth, P. A. Nekludova, S. V. Sokolov, A. A. Elistratov, D. R. Yakovlev, M. Bayer, A. V. Akimov, and A. V. Scherbakov, Generation of a localized microwave magnetic field by coherent phonons in a ferromagnetic nanograting, *Phys. Rev. B* **97**, 060404(R) (2018).
- [34] M. Inoue, A. Baryshev, H. Takagi, P. B. Lim, K. Hatafuku, J. Noda, and K. Togo, Investigating the use of magnonic crystals as extremely sensitive magnetic field sensors at room temperature, *Appl. Phys. Lett.* **98**, 132511 (2011).
- [35] M. Bombeck, A. S. Salasyuk, B. A. Glavin, A. V. Scherbakov, C. Brüggemann, D. R. Yakovlev, V. F. Sapega, X. Liu, J. K. Furdyna, A. V. Akimov, and M. Bayer, Excitation of spin waves in ferromagnetic (ga,mn)as layers by picosecond strain pulses, *Phys. Rev. B* **85**, 195324 (2012).
- [36] R. Verba, I. Lisenkov, I. Krivorotov, V. Tiberkevich, and A. Slavin, Nonreciprocal surface acoustic waves in multilayers with magnetoelastic and interfacial Dzyaloshinskii-Moriya interactions, *Phys. Rev. Appl.* **9**, 064014 (2018).
- [37] F. Godejohann, A. V. Scherbakov, S. M. Kukhtaruk, A. N. Poddubny, D. D. Yaremkevich, M. Wang, A. Nadzeyka, D. R. Yakovlev, A. W. Rushforth, A. V. Akimov, and M. Bayer, Magnon polaron formed by selectively coupled coherent magnon and phonon modes of a surface patterned ferromagnet, *Phys. Rev. B* **102**, 144438 (2020).
- [38] R. W. Damon and J. R. Eshbach, Magnetostatic modes of a ferromagnet slab, *J. Phys. Chem. Solids* **19**, 308 (1961).
- [39] T. Schneider, A. A. Serga, T. Neumann, B. Hillebrands, and M. P. Kostylev, Phase reciprocity of spin-wave excitation by a microstrip antenna, *Phys. Rev. B* **77**, 214411 (2008).
- [40] M. Kostylev, Non-reciprocity of dipole-exchange spin waves in thin ferromagnetic films, *J. Appl. Phys.* **113**, 053907 (2013).
- [41] M. Mruczkiewicz, P. Graczyk, P. Lupo, A. Adeyeye, G. Gubbiotti, and M. Krawczyk, Spin-wave nonreciprocity and magnonic band structure in a thin permalloy film induced by dynamical coupling with an array of ni

- stripes, *Phys. Rev. B* **96**, 104411 (2017).
- [42] G. Gubbiotti, A. Sadovnikov, E. Beginin, S. Nikitov, D. Wan, A. Gupta, S. Kundu, G. Talmelli, R. Carpenter, I. Asselberghs, I. P. Radu, C. Adelman, and F. Ciubotaru, Magnonic band structure in vertical meander-shaped $\text{Co}_{40}\text{Fe}_{40}\text{B}_{20}$ thin films, *Phys. Rev. Applied* **15**, 014061 (2021).
- [43] M. Farle, Ferromagnetic resonance of ultrathin metallic layers, *Reports on Progress in Physics* **61**, 755 (1998).
- [44] R. E. De Wames and T. Wolfram, Dipole-exchange spin waves in ferromagnetic films, *Journal of Applied Physics* **41**, 987 (1970).
- [45] W. K. Hiebert, A. Stankiewicz, and M. R. Freeman, Direct observation of magnetic relaxation in a small permalloy disk by time-resolved scanning Kerr microscopy, *Phys. Rev. Lett.* **79**, 1134 (1997).
- [46] M. van Kampen, C. Jozsa, J. T. Kohlhepp, P. LeClair, L. Lagae, W. J. M. de Jonge, and B. Koopmans, All-optical probe of coherent spin waves, *Phys. Rev. Lett.* **88**, 227201 (2002).
- [47] V. N. Kats, T. L. Linnik, A. S. Salasyuk, A. W. Rushforth, M. Wang, P. Wadley, A. V. Akimov, S. A. Cavill, V. Holy, A. M. Kalashnikova, and A. V. Scherbakov, Ultrafast changes of magnetic anisotropy driven by laser-generated coherent and incoherent phonons in metallic films, *Phys. Rev. B* **93**, 214422 (2016).
- [48] A. V. Scherbakov, A. P. Danilov, F. Godejohann, T. L. Linnik, B. A. Glavin, L. A. Shelukhin, D. P. Pattnaik, M. Wang, A. W. Rushforth, D. R. Yakovlev, A. V. Akimov, and M. Bayer, Optical excitation of single- and multimode magnetization precession in Fe-Ga nanolayers, *Phys. Rev. Applied* **11**, 031003 (2019).
- [49] N. E. Khokhlov, P. I. Gerevenkov, L. A. Shelukhin, A. V. Azovtsev, N. A. Pertsev, M. Wang, A. W. Rushforth, A. V. Scherbakov, and A. M. Kalashnikova, Optical excitation of propagating magnetostatic waves in an epitaxial gallenol film by ultrafast magnetic anisotropy change, *Phys. Rev. Applied* **12**, 044044 (2019).
- [50] COMSOL Multiphysics[®] v. 5.4. www.comsol.com. COMSOL AB, Stockholm, Sweden.
- [51] E. M. Lifshitz and L. P. Pitaevskii, *Statistical Physics, Part 2: Theory of the Condensed State*, Vol. 9 (Butterworth-Heinemann, 1980).
- [52] V. G. Bar'yakhtar, Phenomenological description of relaxation processes in magnetic materials, *Zh. Eksp. Teor. Fiz.* **87**, 1501 (1984).
- [53] O. Chubykalo-Fesenko, U. Nowak, R. W. Chantrell, and D. Garanin, Dynamic approach for micromagnetics close to the curie temperature, *Phys. Rev. B* **74**, 094436 (2006).
- [54] See Supplemental Material below for details related to the static demagnetizing field of the nanogratings, magnons in nanogratings for DE and BV geometries, spatial Fourier transform of magnon modes, and the verification of micromagnetic simulations using COMSOL Multiphysics.
- [55] Alternatively, the Fourier transform can be performed separately in the wire and groove regions. In this case there are two "magnon quantum numbers" to characterize the magnons [25].
- [56] W. G. Yang, M. Jaris, C. Berk, and H. Schmidt, Preferential excitation of a single nanomagnet using magnetoelectric coupling, *Phys. Rev. B* **99**, 104434 (2019).
- [57] N. K. P. Babu, A. Trzaskowska, P. Graczyk, G. Centala, S. Mieszczyk, H. Głowiński, M. Zdunek, S. Mielcarek, and J. W. Klos, The interaction between surface acoustic waves and spin waves: The role of anisotropy and spatial profiles of the modes, *Nano Letters* **21**, 946 (2021).
- [58] B. A. Kalinikos and A. N. Slavin, Theory of dipole-exchange spin wave spectrum for ferromagnetic films with mixed exchange boundary conditions, *Journal of Physics C: Solid State Physics* **19**, 7013 (1986).
- [59] R. A. Gallardo, A. Banholzer, K. Wagner, M. Körner, K. Lenz, M. Farle, J. Lindner, J. Fassbender, and P. Landeros, Splitting of spin-wave modes in thin films with arrays of periodic perturbations: theory and experiment, *New Journal of Physics* **16**, 023015 (2014).
- [60] μ MAG, Micromagnetic Modeling Activity Group, www.ctcms.nist.gov/~rdm/mumag.org.html.
- [61] Q. Wang, X. Li, C.-Y. Liang, A. Barra, J. Dommann, C. Lynch, A. Sepulveda, and G. Carman, Strain-mediated 180° switching in *cofeb* and *terfenol-d* nanodots with perpendicular magnetic anisotropy, *Applied Physics Letters* **110**, 102903 (2017).
- [62] S. Manna, J. W. Kim, M. V. Lubarda, J. Wingert, R. Harder, F. Spada, V. Lomakin, O. Shpyrko, and E. E. Fullerton, Characterization of strain and its effects on ferromagnetic nickel nanocubes, *AIP Advances* **7**, 125025 (2017).
- [63] V. A. Bautin, A. G. Seferyan, M. S. Nesmeyanov, and N. A. Usov, Magnetic properties of polycrystalline cobalt nanoparticles, *AIP Advances* **7**, 045103 (2017).
- [64] H.-G. Piao, H.-C. Choi, J.-H. Shim, D.-H. Kim, and C.-Y. You, Ratchet effect of the domain wall by asymmetric magnetostatic potentials, *Applied Physics Letters* **99**, 192512 (2011).
- [65] D. B. Gopman, V. Sampath, H. Ahmad, S. Bandyopadhyay, and J. Atulasimha, Static and dynamic magnetic properties of sputtered Fe-Ga thin films, *IEEE Trans. Mag.* **53**, 1 (2017).
- [66] S. Klingler, A. V. Chumak, T. Mewes, B. Khodadadi, C. Mewes, C. Dubs, O. Surzhenko, B. Hillebrands, and A. Conca, Measurements of the exchange stiffness of YIG films using broadband ferromagnetic resonance techniques, *Journal of Physics D: Applied Physics* **48**, 015001 (2014).
- [67] D. D. Awschalom, C. R. Du, R. He, F. J. Heremans, A. Hoffmann, J. Hou, H. Kurebayashi, Y. Li, L. Liu, V. Novosad, J. Sklenar, S. E. Sullivan, D. Sun, H. Tang, V. Tyberkevych, C. Trevillian, A. W. Tsien, L. R. Weiss, W. Zhang, X. Zhang, L. Zhao, and C. W. Zollitsch, Quantum engineering with hybrid magnonic systems and materials, *IEEE Transactions on Quantum Engineering* **2**, 1 (2021).
- [68] Y. Li, W. Zhang, V. Tyberkevych, W.-K. Kwok, A. Hoffmann, and V. Novosad, Hybrid magnonics: Physics, circuits, and applications for coherent information processing, *J. Appl. Phys.* **128**, 130902 (2020).
- [69] T. Satoh, Y. Terui, R. Moriya, B. A. Ivanov, K. Ando, E. Saitoh, T. Shimura, and K. Kuroda, Directional control of spin-wave emission by spatially shaped light, *Nat. Photonics* **6**, 662 (2012).
- [70] M. Jäckl, V. I. Belotelov, I. A. Akimov, I. V. Savochkin, D. R. Yakovlev, A. K. Zvezdin, and M. Bayer, Magnon accumulation by clocked laser excitation as source of long-range spin waves in transparent magnetic films, *Phys. Rev. X* **7**, 021009 (2017).

- [71] M. A. W. Schoen, D. Thonig, M. L. Schneider, T. J. Silva, H. T. Nembach, O. Eriksson, O. Karis, and J. M. Shaw, Ultra-low magnetic damping of a metallic ferromagnet, *Nat. Phys.* **21**, 839 (2016).
- [72] H. Yu, R. Huber, T. Schwarze, F. Brandl, T. Rapp, P. Berberich, G. Duerr, and D. Grundler, High propagating velocity of spin waves and temperature dependent damping in a c0feb thin film, *Appl. Phys. Lett.* **100**, 262412 (2012).

Supplemental Material for "Transition magnon modes in thin ferromagnetic nanogratings."

S. M. Kukhtaruk,^{1,2} A. W. Rushforth,³ F. Godejohann,¹ A. V. Scherbakov,¹ and M. Bayer¹

¹*Experimentelle Physik 2, Technische Universität Dortmund,
Otto-Hahn-Str. 4a, 44227 Dortmund, Germany.*

²*Department of Theoretical Physics, V.E. Lashkaryov
Institute of Semiconductor Physics, 03028 Kyiv, Ukraine.*

³*School of Physics and Astronomy, University of Nottingham, Nottingham NG7 2RD, United Kingdom.*

I. STATIC DEMAGNETIZING FIELD OF THE NANOGRATINGS

The nonzero components of \mathbf{H}_d^0 are shown in Fig. S1 for several important directions of H_{ext} . As one can see, both components of \mathbf{H}_d^0 increase with increasing φ_H . For the case of $\varphi_H = 90^\circ$ the arrows of the demagnetizing vector field are introduced. Figure S1(a) shows that $H_{d,x}^0$ is negative in the wire region and positive in the groove region of the NG, which considerably affects the orientation of the magnetization. It is worth emphasizing that the demagnetizing field is nonzero outside the nanograting.

The symmetry of \mathbf{H}_d^0 with respect to the center of the NG wire region for the $x \rightarrow -x$ operation in the steady-state is given by Eq. 4 of the main text. The demagnetizing field imposes different symmetry for the in-plane and out-of-plane magnetization components. Moreover, the symmetry of the i -th component of the magnetization reflects the symmetry of the i -th non-zero component of the demagnetizing field ($i = x, y, z$). In the case of an in-plane \mathbf{H}_{ext} , $m_x^0(x, z)$ and $m_z^0(x, z)$ are even and odd functions, respectively (see below). Furthermore, the numerator of the integrand in Eq. 4 consists of the odd functions $m_x^0(x - x')$ and $m_z^0(z - z')$ (one needs to change also $x' \rightarrow -x'$). Thus, $H_{d,x}^0$ is an even, and $H_{d,z}^0$ is an odd function, respectively. Similarly, one obtains opposite symmetry properties if the magnetization is parallel to the z -direction. In the case of an arbitrary out-of-plane orientation of the magnetization, both \mathbf{m}^0 and \mathbf{H}_d^0 are neither symmetric nor antisymmetric functions.

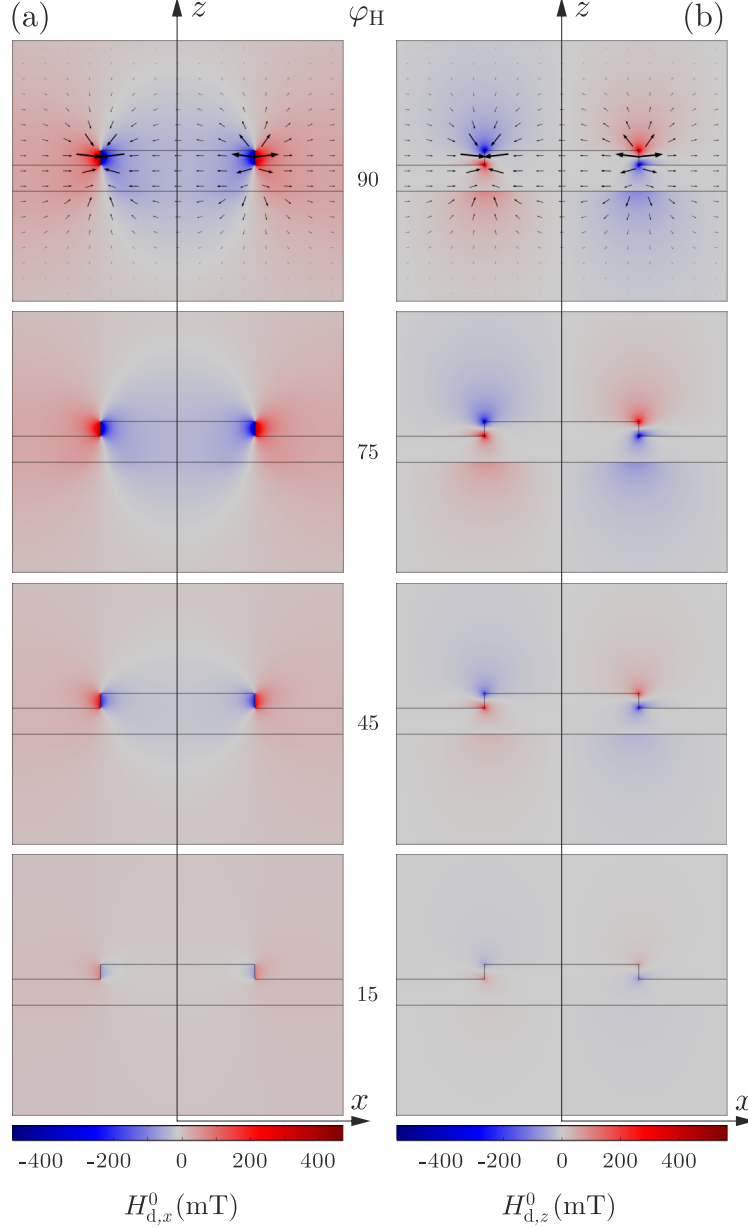


Figure S1. Spatial distributions of the (a) x -components and (b) z -components of the static demagnetizing field \mathbf{H}_d^0 for different directions of \mathbf{H}_{ext} at $H_{\text{ext}} = 200$ mT. The values of φ_H are shown in between (a) and (b) in degrees. In the case of $\varphi_H = 90^\circ$ arrows represent the demagnetizing vector field. The length of the arrows is proportional to $|\mathbf{H}_d^0|$ in the center of each arrow.

II. MAGNONS IN NANOGRATINGS FOR DAMON-ESHBACH AND BACKWARD-VOLUME GEOMETRIES

The magnetic field dependencies of the magnon frequencies in nanogratings for both the backward-volume (BV) and Damon-Eshbach (DE) geometries have been already reported in [S1]. In this work, we complement these dependencies by additional antisymmetric magnon modes which cannot be accessed using a symmetric excitation and detection scheme [S1], and higher order modes. For the calculations, all parameters are chosen as they were introduced in the main

text.

Figure S2(a) shows the magnetic field dependence of the magnon frequencies in the DE geometry, i.e. $\varphi_H = 0^\circ$. The presented dependence is similar as for the magnon modes in thin ferromagnetic films for magnetization directions close to the easy axis, because the static demagnetizing field is zero [S1, S2] (see also the Sec. II in the main text).

The magnetic field dependence of the magnon frequencies in the BV geometry ($\varphi_H = 90^\circ$) is shown in Fig. S2(b). The corresponding inset shows the magnetic field dependence of the average steady-state in-plane magnetization angle $\bar{\varphi}_M$, indicating the saturation magnetic field at ≈ 73 mT. For H_{ext} smaller than the saturation magnetic field, one can observe a complicated non-monotonic behavior with magnon-magnon interaction and corresponding avoided crossings. For $H_{\text{ext}} > 73$ mT the behavior is much simpler and in most cases the magnon frequencies monotonically grow with increasing H_{ext} .

Figures S3(a), (b) show the results of micromagnetic simulations for the DE geometry ($\varphi_H = 0^\circ$). For this field direction, $\bar{\varphi}_M = \varphi_H$, because the static demagnetizing field is zero [S2]. From Fig. S3(a) one can see that all magnon branches are nonreciprocal, i.e. $\omega(k_x) \neq \omega(-k_x)$, except for the ground one. Moreover, indirect band gaps arise.

Figure S3(b) shows magnon modes' spatial profiles which correspond to the center of the Brillouin zone at $k_x = 0$. The ground magnon mode is quasiuniform. The next two modes are symmetric and antisymmetric magnon modes with $k_x = 2\pi/d$. The following modes are higher-order magnon modes. Magnon modes with wave vectors corresponding to the center of the Brillouin zone are propagating waves. Their group velocities $v_g = \frac{d\omega}{dk_x}$ are defined by the slopes of the dispersion curves. As an example, see Supplemental Video I, where the third mode corresponding to $k_x = 0$ and possessing a negative group velocity, is visualized and its motion in the negative x -direction is clearly seen.

Figures S3(c), (d) show magnon modes' dispersion curves and their spatial profiles in the BV geometry ($\varphi_H = 90^\circ$). One can see, that this case drastically differs from the case of the DE geometry. In Fig. S3(c), all modes are reciprocal. The first eleven dispersion branches are nearly

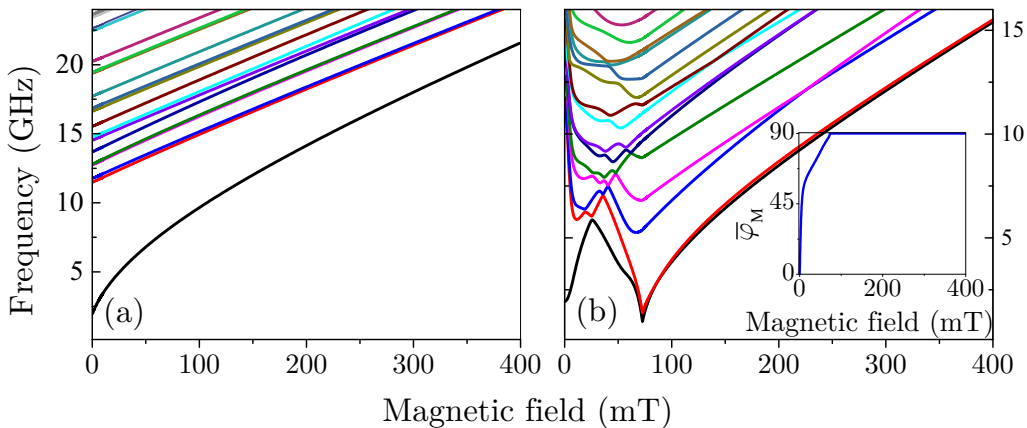


Figure S2. Magnetic field dependencies of the magnon frequencies for the case of (a) the DE geometry ($\varphi_H = 0^\circ$) and (b) the BV geometry ($\varphi_H = 90^\circ$). The inset in (b) shows the magnetic field dependence of the average steady-state in-plane magnetization angle $\bar{\varphi}_M$. Note, that the vertical scales in (a) and (b) are different. The magnon mode branches correspond to the center of the Brillouin zone. The color schemes of the lines here, below and in the main text are the same.

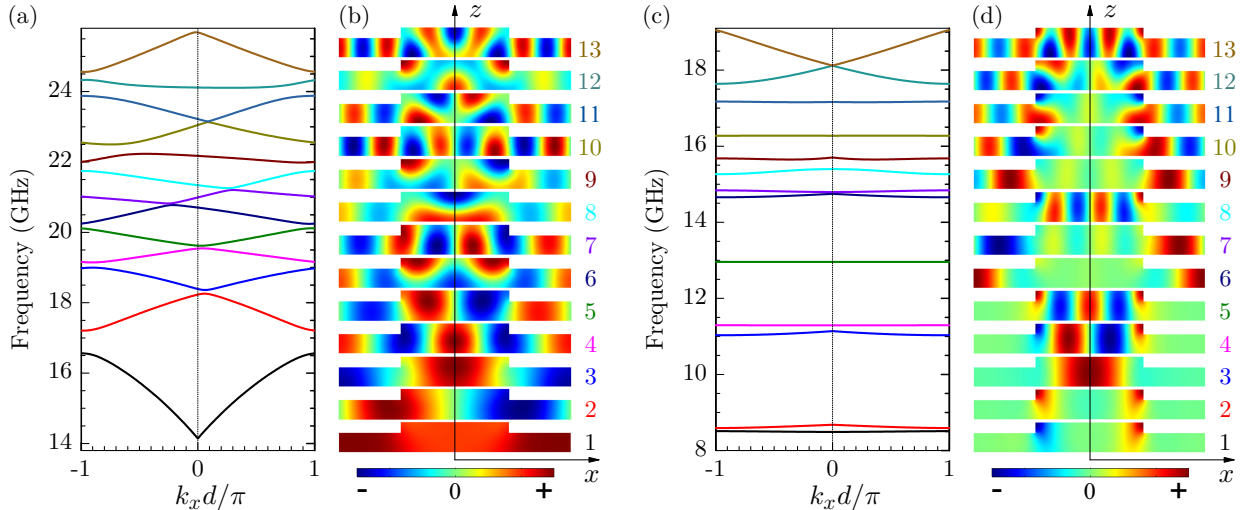


Figure S3. Magnon dispersions and mode profiles at $H_{\text{ext}} = 200$ mT in (a), (b) the DE geometry and (c), (d) the BV geometry. (a), (c) Magnon dispersion curves. The vertical dotted line in (a), (c) at $k_x = 0$ indicates the center of the Brillouin zone. (b), (d) Spatial profiles of the magnon modes at $k_x = 0$ in the unit cell of the NG. The colored numbers correspond to the magnon dispersion branches.

flat [S1, S3]. Moreover, the existence of huge band gaps in their frequency spectrum is worth of mention. The largest three band gaps are between the second and third, fourth and fifth, and fifth and sixth magnon branches possessing values of 2.35 GHz, 1.67 GHz, and 1.7 GHz, respectively.

Figure S3(d) shows magnon modes' spatial profiles which correspond to the center of the Brillouin zone at $k_x = 0$. In the BV geometry all modes are standing waves due to the reciprocal dispersion. The first two modes are antisymmetric and symmetric edge modes. The next three are so-called wire modes. The 6-th and 7-th modes are symmetric and antisymmetric groove modes [S1]. An example of wire mode oscillations can be found in the Supplemental Video II.

The presented results in Fig. S2 are perfectly consistent with previously reported experimental (FMR) and numerical results [S1]. For the DE geometry, Fig. S2(b) has to be compared to Fig. 7 in [S1]. For the case of the BV geometry, Fig. S2(a) has to be compared to Fig. 5(d), (h) in [S1]. Note, that in this work the number of lines is larger than in [S1], because Fig. S2 shows both symmetric and antisymmetric magnon modes.

III. SPATIAL FOURIER TRANSFORM OF MAGNON MODES

Figure S4 shows the results of spatial Fourier transforms of the magnon modes' spatial profiles for different directions of the external magnetic field. For instance, Fig. S4(a) for $\varphi_H = 0^\circ$ shows that the value of the Fourier amplitude at $n = 0$ is much larger than the values for other n . That is, this mode is a quasiuniform magnon mode. Similarly, Figs. S4 (b), (c) for $\varphi_H = 0$ show modes with $n = 1$ and $n = 2$, respectively. In the BV geometry, the magnon modes are characterized by several values of n . In the transition range, i.e. from $\varphi_H \approx 50^\circ$ to $\approx 75^\circ$ the spectral composition considerably differs from the spectral composition at $\varphi_H = 90^\circ$. The sharp peaks are caused by magnon-magnon interactions with other magnon modes.

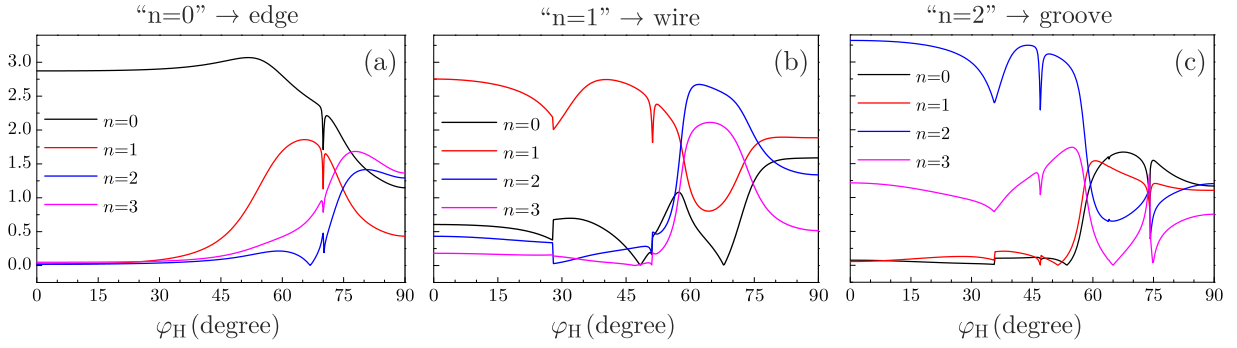


Figure S4. Dependencies of the spatial Fourier amplitudes for the main harmonics on the external magnetic field direction for the transition of (a) "n = 0 mode" to the edge mode; (b) "n = 1 mode" to the wire mode; (c) "n = 2 mode" to the groove mode.

IV. VERIFICATION OF MICROMAGNETIC SIMULATIONS USING COMSOL MULTIPHYSICS

In reference [S4] five μMAG standard problems of micromagnetics can be found. Among all of them, problem #4 deals with the case of a spatially nonhomogeneous, time-dependent magnetization precession in a thin Permalloy plate. Due to the link to the treated system in this work, in the following, the problem is formulated and solved using COMSOL Multiphysics[®] [S5] (Comsol). In order to verify the accuracy of the solved problem using Comsol, a comparison with different solutions given in [S4] is discussed.

We want to emphasize, that we are not claiming the novelty of utilizing Comsol for micromagnetic simulations (see e.g. [S6, S7]). However, as far as micromagnetics is not a default module of Comsol we decided to verify our implementation of micromagnetics to Comsol by solving the standard micromagnetic problems.

The object of our study is given by the Permalloy plate, which is illustrated in Fig. S5. The used parameters are $L = 500$ nm, $d = 125$ nm and $t = 3$ nm. We take the same Permalloy material parameters as used in [S4] only in this section of the Supplemental Material. It is important to emphasize that these parameters are different from the values in reference [S1], which have been used in the main text. Hence, the exchange stiffness constant is $D = 3.25 \cdot 10^{-17}$ Tm². The saturation magnetization is $M_s = 1.0053$ T, and the Gilbert damping constant is $\alpha = 0.02$.

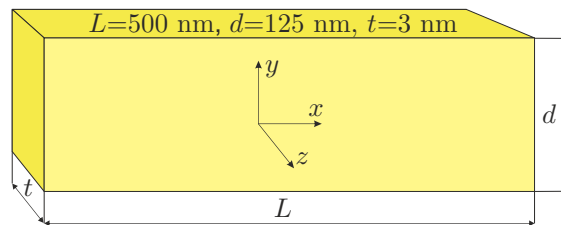


Figure S5. Sketch of the geometry of the micromagnetic problem (not to scale!).

The first part of the solution of problem #4 is given by the calculation of the so-called s-state, which is the specific steady-state spatial distribution of the magnetization (see Fig. S6(a)). In order to do so, a saturating magnetic field is applied along the [111]-crystallographic direction and,

subsequently, slowly decreased to zero. As one can see in Fig. S6, the calculated s-state using Comsol looks very similar to the results taken from [S4] (see Fig. S6(b)). The resulting s-state determines the initial state for the solution of the second part of problem #4, which deals with the time evolution of the magnetization.

For the second part of problem #4, another magnetic field is applied along the opposite direction of the equilibrium magnetization of the s-state in order to change the magnetization orientation. The main aim is to track the time evolution of the magnetization towards the new magnetic field direction [S4]. The applied magnetic field is given by $H_x = -24.6$ mT, $H_y = -4.3$ mT, and $H_z = 0.0$ mT. In other words, the magnetic field strength of ≈ 25 mT is directed 170 degrees counterclockwise relative to the positive x -axis in the x - y plane.

In this paragraph, we present the details of the calculation in Comsol which could be useful for Comsol users. For the magnetic field calculation we used the "AC/DC" module ("Magnetic Fields, No Currents"). The Landau-Lifshits-Gilbert equation was implemented using the basic module of Comsol i.e. "Mathematics" ("Coefficient form PDE"). We introduce an air sphere of $2 \mu\text{m}$ radius around the Permalloy plate with a 200-nm thick external layer of "infinite element domain". The magnetic scalar potential on the surface of the sphere is set to zero. The maximum element size in the plate is set to 5 nm. For the sphere, we choose an "extremely coarse" mesh. We used the quartic Lagrange discretization in the Coefficient form PDE and quadratic in the "Magnetic Fields, No Currents". The maximum time step is taken as 0.5 ps.

Figure S7 summarizes the calculated time-dependent spatially averaged magnetization components by our and other groups. Fig. S7(a) shows the comparison of the results obtained using Comsol (lines) and using a finite difference software developed by E. Martinez, L. Torres and L. Lopez-Diaz (dots). One can see a very good agreement between the calculated lines and dots. Another comparison of the results using Comsol and using the finite difference software developed by J. L. Martins and T. Rocha is presented in Fig. S7(b). In this case, perfect agreement between both calculations is observed. The discrepancy between the different calculations is due to the fact that the exact analytical solution of the considered problem is unknown. Thus, different approaches, different mesh sizes, etc., give slightly different results.

We want to emphasize, that the calculated amplitude of precession is on the order of the saturation magnetization (see Fig. S7), which is much larger than in usual experiments investigating

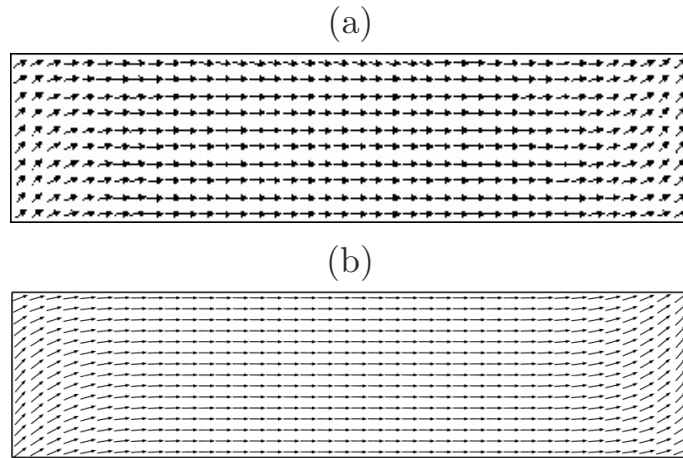


Figure S6. Steady-state spatial distribution of the magnetization in the s-state: (a) taken from [S4]; (b) Comsol calculations.

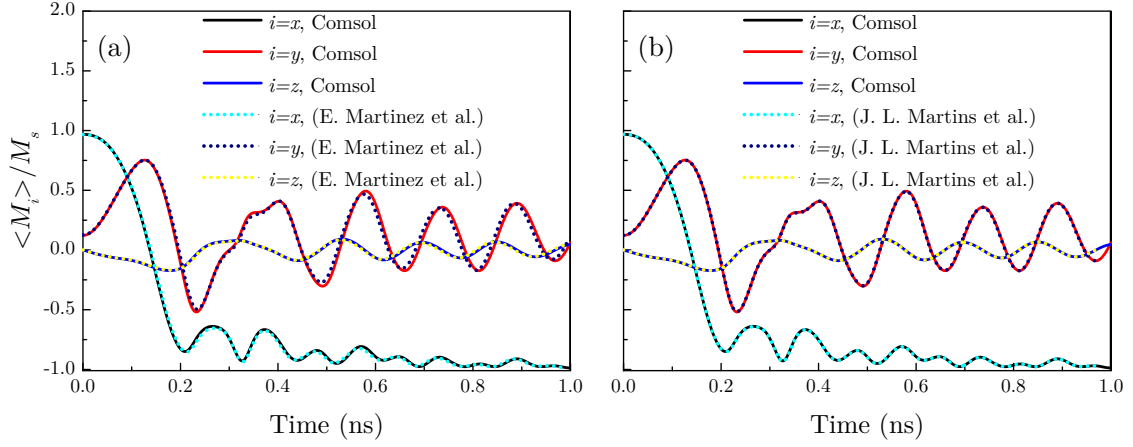


Figure S7. Comparison of results of micromagnetic calculations which were obtained with Comsol and results from the groups of (a) E. Martinez et al. (data for 2.5 nm mesh size [S4]) and (b) J. L. Martins et al. (data for 1 nm mesh size [S4]).

magnons (see e.g. [S8–S11]). Hence, the three-dimensional problem #4 is strongly nonlinear and reflects a case, which is much more complicated than the simulation of magnons in effectively two-dimensional gratings with precession amplitudes much smaller than M_s .

The last validation of the solution of problem #4 is provided by the comparison of the spatial distribution of the magnetization at the time, when the x -component of the spatially averaged magnetization first crosses zero (≈ 0.1375 ns). In Fig. S8(a) one can see the spatial distribution which was calculated by M. J. Donahue and D. G. Porter, using the OOMMF eXtensible solver [S4], while Fig. S8(b) shows the spatial distribution of the magnetization using Comsol. Besides the different colors, there is good agreement between both calculated distributions.

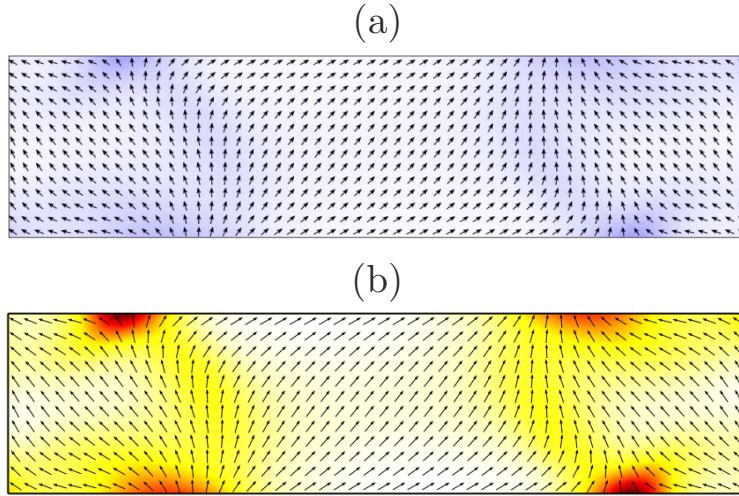


Figure S8. Spatial distribution of the magnetization at the time = 0.1375 ns (see Fig. S7). Distribution (a) is calculated by M. J. Donahue et al., using the OOMMF software, and distribution (b) is calculated using Comsol. The background color indicates the z component of the magnetization.

[S1] M. Langer, R. A. Gallardo, T. Schneider, S. Stienen, A. Roldán-Molina, Y. Yuan, K. Lenz, J. Lindner, P. Landeros, and J. Fassbender, Spin-wave modes in transition from a thin film to a full magnonic

- crystal, *Phys. Rev. B* **99**, 024426 (2019).
- [S2] I. Lisenkov, D. Kalyabin, S. Osokin, J. W. Klos, M. Krawczyk, and S. Nikitov, Nonreciprocity of edge modes in 1d magnonic crystal, *J. Magn. Magn. Mater.* **378**, 313 (2015).
- [S3] R. A. Gallardo, T. Schneider, A. Roldán-Molina, M. Langer, J. Fassbender, K. Lenz, J. Lindner, and P. Landeros, Dipolar interaction induced band gaps and flat modes in surface-modulated magnonic crystals, *Phys. Rev. B* **97**, 144405 (2018).
- [S4] μ MAG, Micromagnetic Modeling Activity Group, www.ctcms.nist.gov/~rdm/mumag.org.html.
- [S5] COMSOL Multiphysics[®] v. 5.4. www.comsol.com. COMSOL AB, Stockholm, Sweden.
- [S6] M. Mruczkiewicz, M. Krawczyk, V. K. Sakharov, Y. V. Khivintsev, Y. A. Filimonov, and S. A. Nikitov, Standing spin waves in magnonic crystals, *J. Appl. Phys.* **113**, 093908 (2013).
- [S7] J. Rychly, P. Gruszecki, M. Mruczkiewicz, J. W. Klos, S. Mamica, and M. Krawczyk, Magnonic crystals – prospective structures for shaping spin waves in nanoscale, *Low Temperature Physics* **41**, 745 (2015).
- [S8] M. van Kampen, C. Jozsa, J. T. Kohlhepp, P. LeClair, L. Lagae, W. J. M. de Jonge, and B. Koopmans, All-optical probe of coherent spin waves, *Phys. Rev. Lett.* **88**, 227201 (2002).
- [S9] V. N. Kats, T. L. Linnik, A. S. Salasyuk, A. W. Rushforth, M. Wang, P. Wadley, A. V. Akimov, S. A. Cavill, V. Holy, A. M. Kalashnikova, and A. V. Scherbakov, Ultrafast changes of magnetic anisotropy driven by laser-generated coherent and noncoherent phonons in metallic films, *Phys. Rev. B* **93**, 214422 (2016).
- [S10] A. S. Salasyuk, A. V. Rudkovskaya, A. P. Danilov, B. A. Glavin, S. M. Kukhtaruk, M. Wang, A. W. Rushforth, P. A. Nekludova, S. V. Sokolov, A. A. Elistratov, D. R. Yakovlev, M. Bayer, A. V. Akimov, and A. V. Scherbakov, Generation of a localized microwave magnetic field by coherent phonons in a ferromagnetic nanograting, *Phys. Rev. B* **97**, 060404(R) (2018).
- [S11] A. V. Scherbakov, A. P. Danilov, F. Godejohann, T. L. Linnik, B. A. Glavin, L. A. Shelukhin, D. P. Pattnaik, M. Wang, A. W. Rushforth, D. R. Yakovlev, A. V. Akimov, and M. Bayer, Optical excitation of single- and multimode magnetization precession in Fe-Ga nanolayers, *Phys. Rev. Applied* **11**, 031003 (2019).